ECS Journal of Solid State Science and Technology, **6** (12) N243-N249 (2017)

Atmospheric Pressure Plasma Enhanced Spatial ALD of ZrO_2 for Low-Temperature, Large-Area Applications

Maria A. Mione,[a,b,z] Ilias Katsouras,[a] Yves Creyghton,[a] Willem van Boekel,[a] Joris Maas,[a] Gerwin Gelinck,[a,b] Fred Roozeboom,[a,b,*] and Andrea Illiberi[a,c]

[a]*TNO/Holst Centre, High Tech Campus 31, 5656AE Eindhoven, The Netherlands*
[b]*Department of Applied Physics, Eindhoven University of Technology, 5600 MB Eindhoven, The Netherlands*

High permittivity (high-k) materials have received considerable attention as alternatives to SiO_2 for CMOS and low-power flexible electronics applications. In this study, we have grown high-quality ZrO_2 by using atmospheric-pressure plasma-enhanced spatial ALD (PE-sALD), which, compared to temporal ALD, offers higher effective deposition rates and uses atmospheric-pressure plasma to activate surface reactions at lower temperatures. We used tetrakis(ethylmethylamino)zirconium (TEMAZ) as precursor and O_2 plasma as co-reactant at temperatures between 150 and 250°C. Deposition rates as high as 0.17 nm/cycle were achieved with N- and C- contents as low as 0.4% and 1.5%, respectively. Growth rate, film crystallinity and impurity contents in the films were found to improve with increasing deposition temperature. The measured relative permittivity lying between 18 and 28 with leakage currents in the order of 5×10^{-8} A/cm^2 demonstrates that atmospheric PE-sALD is a powerful technique to deposit ultrathin, high-quality dielectrics for low-temperature, large-scale microelectronic applications.
© The Author(s) 2017. Published by ECS. This is an open access article distributed under the terms of the Creative Commons Attribution Non-Commercial No Derivatives 4.0 License (CC BY-NC-ND, http://creativecommons.org/licenses/by-nc-nd/4.0/), which permits non-commercial reuse, distribution, and reproduction in any medium, provided the original work is not changed in any way and is properly cited. For permission for commercial reuse, please email: oa@electrochem.org. [DOI: 10.1149/2.0381712jss]

Manuscript submitted October 25, 2017; revised manuscript received November 30, 2017. Published December 23, 2017.

The continuous improvement in performance of integrated circuits has been based on miniaturization of components. The effective gate length in field-effect transistors shrinks to smaller and smaller sizes and, consequently, the thickness of the gate oxide decreases.[1] SiO_2 has been the most popular gate oxide material used in microelectronic manufacturing due to its thermal stability and ideal interface quality on Si. However, during the past fifty years the thickness of the SiO_2 gate oxide has already been reduced to its physical limit of 1.2 nm, below which a critical gate leakage of 1 A/cm^2 is exceeded.[2] To overcome this problem, dielectrics with a high permittivity (high-*k* materials) have been extensively investigated as promising substitutes of the conventional SiO_2 for CMOS and DRAM technology. The high permittivity ($k > 10$) ensures high capacitance for thicker gate oxide layers while greatly reducing tunneling and gate leakage currents.[3,4] Among high-*k* oxides, ZrO_2 is considered one of the most promising SiO_2 alternatives due to its high dielectric constant ($k = 20$–25), large bandgap (5.1–7.8 eV) and thermodynamical stability.[5,6] ZrO_2 proved to be a good dielectric in transistor applications with leakage current of the order of 10^{-6}-10^{-9} A/cm^2 and in DRAM capacitor applications especially when present in $ZrO_2/Al_2O_3/ZrO_2$ nanolaminate structures.[7] High-*k* materials are also relevant for low-power applications of flexible electronics.[5,8–11]

High-*k* materials are deposited in a variety of chemical and physical deposition techniques including metallorganic chemical vapor deposition (MOCVD), atomic layer deposition (ALD), sol-gel and sputtering. ALD has proven to be the most suitable technique for high-*k* deposition due to its unique nanoscale thickness and layer uniformity control. In its conventional time-sequenced mode, ALD is a gas phase deposition technique in which the substrate surface is exposed alternatively to the precursor and reactant vapors in a cyclic and thermally activated manner.[12] Recently, plasma-enhanced ALD has emerged as a deposition technique for low temperature application. The extra energy supplied by plasma radicals to the substrate allows to initiate surface reactions at relatively low temperatures and thus grow materials on flexible and plastic substrates. Conventional and plasma ALD are usually operated in vacuum and they have been extensively reviewed in literature.[12–14] However, conventional vacuum (PE)ALD is not suited for low-cost applications because of its low deposition rate, device size restrictions and high cost. Spatial ALD (sALD), based on a spatial rather than temporal separation of the reaction zones, represents a way to overcome these manufacturing limitations, especially if performed at atmospheric pressure. In spatial ALD continuously flowing precursor and co-reactant are spatially separated by inert gas flows, and the substrate is sequentially exposed to each individual injection zone. Firstly proposed by Suntola et al.,[15] sALD is receiving increasing attention within the industry because of its high throughput in terms of fast rate deposition of high-quality material for large-area applications.[16–22] Therefore, spatial atmospheric-pressure plasma-enhanced ALD uniquely combines the advantages of a fast ALD concept with the possibility of growing insulating and conducting materials at atmospheric conditions and at relatively low temperatures compatible with flexible and temperature sensitive substrates yet without the undesired size restrictions imposed by vacuum systems. Although the use of plasma on substrates with pronounced topographies remains challenging, the advantage of using atmospheric plasma resides in the low kinetic energy of the ionic species, which translates into low ion bombardment and, consequently, reduced ion damage.

Thermal and plasma ALD processes for ZrO_2 films are already known in literature for different classes of precursors and reactants. High-quality films can be grown using halides such as $ZrCl_4$ and ZrI_4, or alkoxides such as $Zr(OtBu)_4$, reacting with H_2O, O_2 and O_2 plasma as reactants,[23–29] as well as zirconium organo-metallic precursors reacting with O_3.[30,31] In particular alkylamide Zr precursors, such as $Zr(NMe)_4$, $Zr(NetMe)_4$, and $Zr(Net_2)_4$, represent a promising choice in view of their high vapor pressure and reactivity with many co-reactants. Besides, most alkylamides are liquid under ambient conditions, thus avoiding contamination problems related to solid precursor chemicals; they do not produce corrosive by-products and, due to the direct Zr-N bond, offer a very low carbon contamination in the final film.[8,25,32–37]

In this paper we report on the deposition of ZrO_2 films using spatial atmospheric plasma-enhanced ALD using tetrakis(ethylmethylamino)zirconium $Zr(NetMe)_4$ (TEMAZ) as the Zr-precursor and N_2-O_2 plasma as the oxidant. As previously reported,[25,34] the use of O_2 plasma is essential to obtain low carbon incorporation in ZrO_2 films at relatively low temperature and, thus, superior device performances. Here, we demonstrate that within the relatively low temperature range of 150–250°C, the growth of ZrO_2 films is strongly enhanced by the use of the plasma. Furthermore, we integrated sALD deposited ZrO_2 layers in metal-insulator-metal (MIM) capacitors and performed current-voltage (I-V) and impedance measurements to extract the breakdown field and the relative permit-

*Electrochemical Society Fellow.
[c]Present address: ASM Belgium, 3001 Leuven, Belgium
[z]E-mail: m.a.mione@tue.nl

Downloaded on 2018-01-02 to IP 80.255.245.234 address. Redistribution subject to ECS terms of use (see ecsdl.org/site/terms_use) unless CC License in place (see abstract).

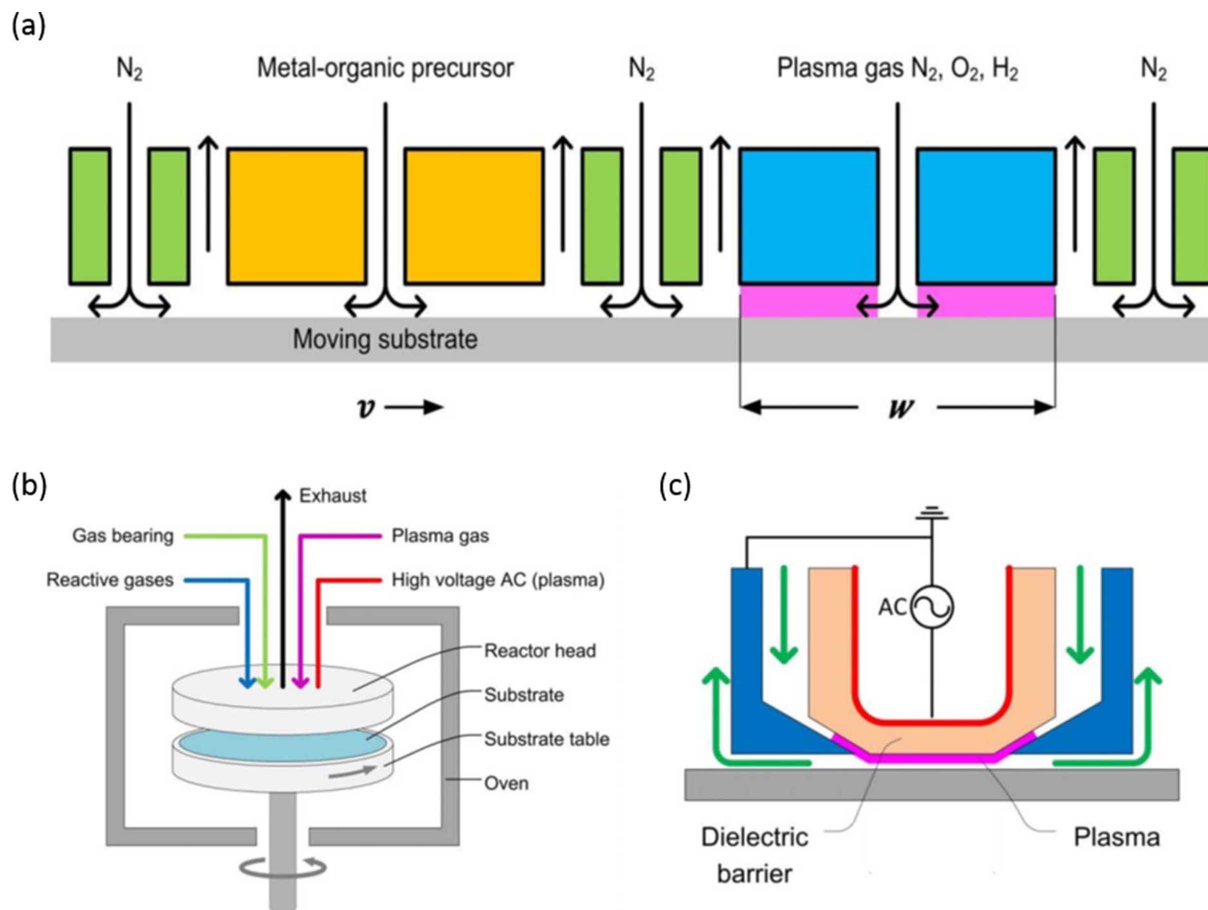

Figure 1. Schematic drawing of the spatial ALD concept. a) Cross-section of the gas injection head with the substrate moving underneath with velocity v so that the two half-reactions will take place sequentially to form metal-oxide monolayers; b) side view of the rotary reactor where the metal-organic precursor and plasma half-reaction zone are separated by N_2 gas bearings; c) Cross-sectional drawing of the direct DBD plasma source.

tivity. We show that the electrical properties of sALD deposited layers are on par with those of layers grown by temporal ALD, with relative permittivity up to 28 and a breakdown field of 4 MV/cm for layers grown at 250°C. The combination of these properties lies on the experimentally observed best-can-do limit.[38]

Experimental

PEALD of ZrO_2 films has been performed in spatial mode at atmospheric pressure using a direct surface Dielectric Barrier Discharge (DBD) based plasma source.[39] A cross-section of the spatial PEALD rotatory reactor previously described[18,40,41] is shown in Figure 1. The rotary sALD reactor has a series of spatially separated zones and the 150-mm c-Si substrate rotates underneath while being exposed sequentially to metal-organic precursor, nitrogen purge, plasma co-reactant and again nitrogen purge. The precursor inlets are surrounded by exhaust outlets through which unreacted precursor and reaction products are removed from the reactor. Series of inlets around the two half-reaction areas provide inert N_2 gas thus serving as the purge steps and avoiding parasitic, CVD-type cross-reactions between coating precursor and oxidant. Also, the inert N_2 serves as a frictionless gas-bearing as a ~100 μm sheet of N_2 which is constantly flowing in the region between the injection head and the substrate. The direct consequence of the gas-bearing system is that the reactor is completely isolated from the environment, allowing for clean processes even at atmospheric pressure.

To generate the plasma a Dielectric Barrier Discharge (DBD) source was used. As indicated in Figure 1c, the plasma is formed between a high voltage and a grounded electrode separated by an insulating dielectric barrier. Reactive plasma species are flow-transported to the surface of the substrate via a 0.3 mm wide slit nozzle. The plasma is generated with an alternating high voltage pulsed power supply, which provides μs pulses of alternating polarity and adjustable amplitude and frequency. The plasma current pulses fall in the range of 0.01–0.1 μs. Typical frequencies are in the 10–100 kHz range. Power density can be varied by adjusting the voltage and the frequency and it is typically of the order of 1–10 W/cm^2.

ZrO_2 depositions were conducted on both c-Si (100) and boron silicate glass substrates using tetrakis(ethylmethylamino)zirconium (TEMAZ) as the precursor and O_2 plasma as the oxidant. The TEMAZ precursor was evaporated from a bubbler heated at 50°C and transported to the reactor chamber by means of heated lines. TEMAZ doses were varied from 0 to 1000 sccm and diluted in 500 sccm of Ar which was employed as the carrier gas. The O_2 flow diluted into 10^4 sccm of N_2 was varied between 0 sccm and 200 sccm. Depositions were performed at different temperatures varying from 150 to 250°C. The exposure time of the substrate to both precursor and oxidant was varied from 82 ms to 655 ms by varying the rotation frequency of the substrate table between 40 and 5 rotations per minute, respectively.

The refractive index (at $\lambda = 632$ nm) and thickness of as-deposited films on c-Si substrates were measured with a J. A. Woollam M2000 rotating compensator ellipsometer using light from a xenon lamp at

Downloaded on 2018-01-02 to IP 80.255.245.234 address. Redistribution subject to ECS terms of use (see ecsdl.org/site/terms_use) unless CC License in place (see abstract).

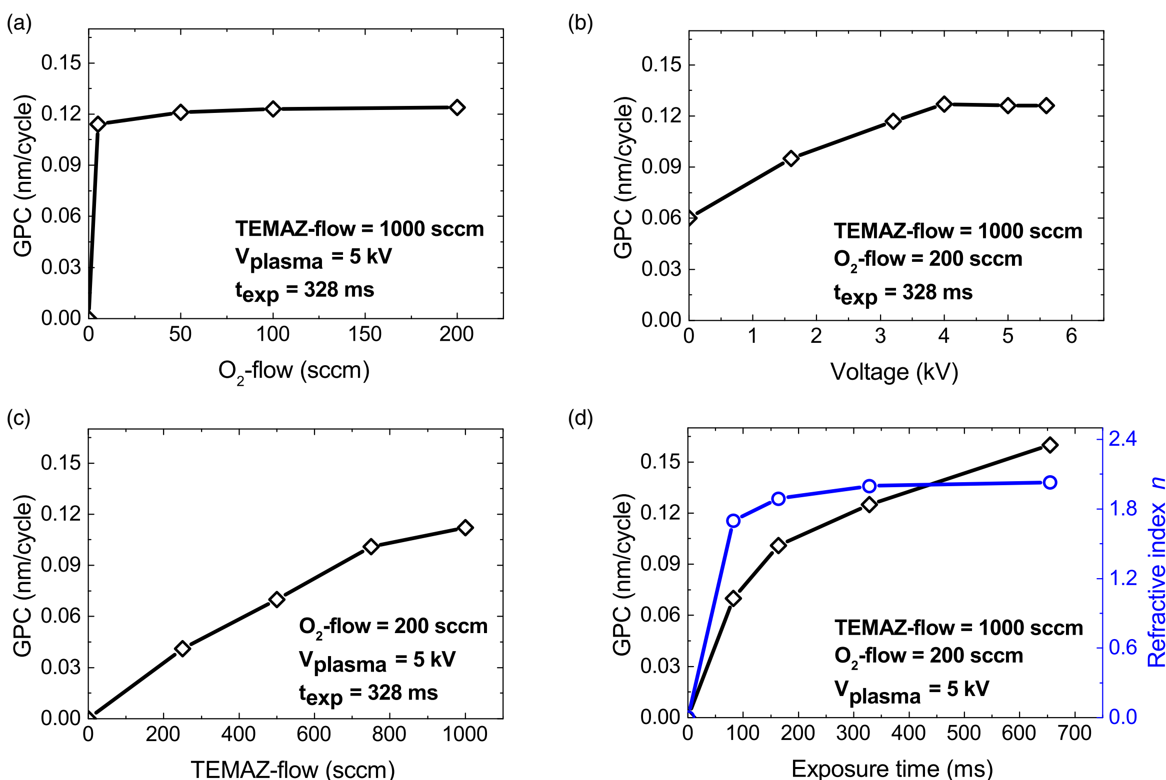

Figure 2. Atmospheric pressure plasma enhanced sALD growth characterization at 150°C deposition temperature. Saturation curves of the GPC as a function of (a) O_2 plasma flow, (b) applied plasma voltage, (c) TEMAZ flow and (d) substrate exposure time t_{exp}. The refractive index n at different exposure times is also shown in (d).

an incidence angle of 75.06°. Film crystallinity has been measured on 100 nm thick films deposited on glass substrates using a Bruker XRD with CuKα radiation (λ = 1.54 Å).

For the electrical characterization, metal-insulator-metal (MIM) capacitors were manufactured on 150 × 150 mm^2 square glass substrates. The capacitors comprised 35–50 nm sALD ZrO_2 layers sandwiched between 100 nm-thick, photo-lithographically patterned electrodes of a molybdenum-chromium alloy. The capacitor area varied between 0.01 cm^2 and 0.000625 cm^2. Measurements of impedance (Z) and phase angle (θ) as a function of frequency were performed with an Agilent E4980A Precision LCR Meter, based on a parallel RC equivalent circuit to extract the data. The leakage and the breakdown field of the capacitors were determined by current-voltage measurements using an Agilent 4155C Semiconductor Parameter Analyzer. All measurements were performed in a probe-station at room temperature and ambient atmosphere.

Results and Discussion

We used a series of plasma-deposited film at the temperature of 150°C to investigate the dependence of the growth per cycle (GPC) on O_2 plasma flow and power, precursor flow and substrate exposure time. The results are presented in Figures 2a–2d. During the growth, the exposure time of the substrate to precursor and oxidant was kept constant at 328 ms and 200 cycles per deposition were used. Under these conditions, by varying O_2 plasma flow (Figure 2a) and applied plasma voltage (Figure 2b), the plasma enhanced s-ALD process exhibits typical self-saturating characteristics and a thermal component accounting for a GPC = 0.06 nm/cycle in the absence of plasma (V = 0 kV).

The TEMAZ flow (Figure 2c) was dosed up to a maximum of 1000 sccm and the GPC curve tends toward saturation for exposure times longer than 655 ms. In the case of TEMAZ and oxygen-based ALD processes at low pressure, several reaction mechanisms have been proposed in literature.[33,42,43] Here, following the simulation work done by Keuter et al. (Ref. 42), which is based on a previous, more elaborate reaction model developed by Weinreich et al. (Ref. 43), we propose the following simplified reaction mechanism. During the first half-cycle, TEMAZ molecules react with OH surface groups in such a way that part of the $N(CH_3)(C_2H_5)$ ligands are oxidized. The precursor adsorption will continue until all the active reaction sites are consumed so that, at the end of the precursor step, the surface is covered by Zr atoms with the remaining unreacted ligands. These ligands are subsequently oxidized by the O_2 plasma reactive species during the second half-cycle. The resulting monolayer consists of ZrO_2 with an OH-terminated surface, which acts as the starting point for the next cycle.[42] Saturation curves for the O_2 flow in Figure 2a reveal that the O_2 plasma is very reactive with the ligand terminated surface at the end of the first half-cycle, and therefore saturation is already achieved with a low flow of 50 sccm. On the contrary, the Zr-precursor (Figure 2c) has a low reactivity with the surface which also limits the saturation curve even at longer exposure times (Figure 2d). This is explained as due to the steric hindrance effect caused by the bulky ligands preventing incoming precursor molecules from reacting with screened yet available surface sites.[42] The expected average thickness of one monolayer of ZrO_2 is 0.3 nm,[44] therefore the GPC presented in Figure 2d suggests that even for high precursor dosing and long exposure time partial monolayer is formed. The refractive index, n, as measured at different exposure times, is also shown in Figure 2d. The film approaches the previously reported[45] value of 2.1 at relatively fast exposure time (328 ms) and saturates beyond 655 ms exposure time.

The same nearly saturated behavior is found at higher deposition temperatures. Figure 3 shows temperature dependent curves at different exposure time. Between 150°C and 250°C, ZrO_2 was deposited

Downloaded on 2018-01-02 to IP 80.255.245.234 address. Redistribution subject to ECS terms of use (see ecsdl.org/site/terms_use) unless CC License in place (see abstract).

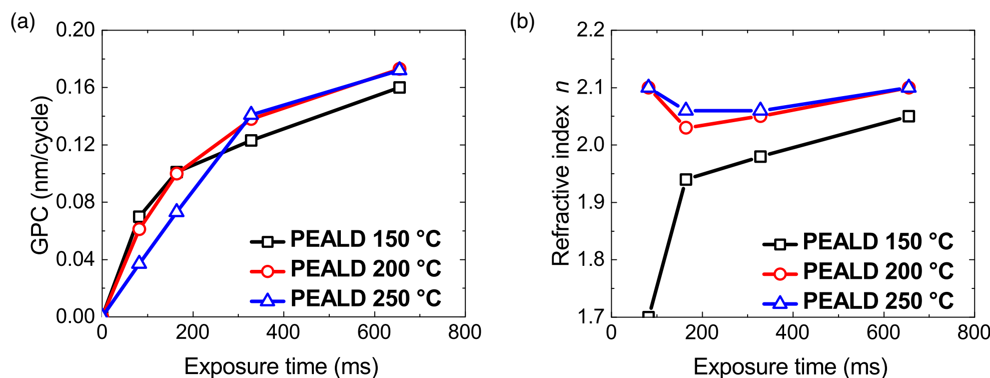

Figure 3. GPC (a) and refractive index (b) as a function of exposure time at different temperatures for plasma-enhanced sALD deposited ZrO_2 films. The TEMAZ-flow is 1000 sccm, the O_2-flow is 200 sccm and the plasma voltage is 5 kV.

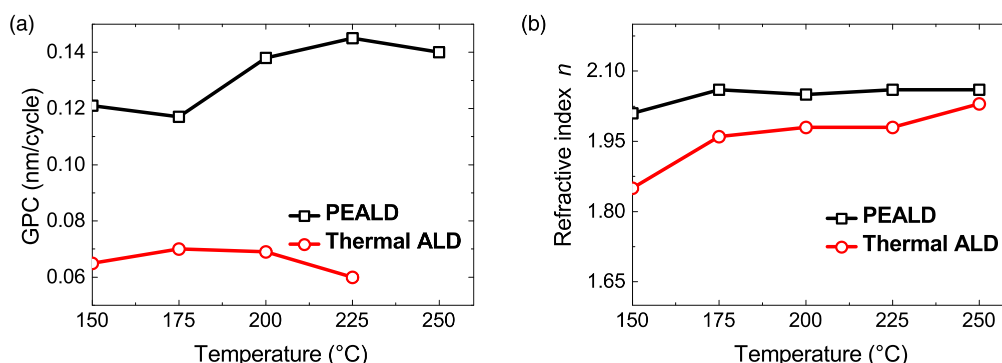

Figure 4. GPC (a) and refractive index (b) as a function of deposition temperature for both plasma enhanced (black squares) and thermal (red circles) sALD grown layers with precursor exposure time of 328 ms. The following conditions for the plasma process have been used: TEMAZ flow = 1000 sccm; O_2-plasma flow = 200 sccm; V_{plasma} = 5 kV.

using an O_2-flow = 200 sccm, a TEMAZ-flow of 1000 sccm and a plasma voltage of 5 kV. The GPC increases due to the higher surface reactivity provided by the higher thermal energy but the saturation is limited by the afore-mentioned steric hindrance effect. A similar trend is observed for the refractive index (Figure 3b). In particular, a general improvement of the refractive index is observed when increasing both exposure time and temperature. This is an indication of the fact that a more dense material is grown when enough thermal energy is provided to the surface and precursor and co-reactant are given sufficient time to react.

Thermal and plasma sALD have been compared at different temperatures. Figure 4 shows the dependence of the GPC and refractive index on the deposition temperature for both thermal and plasma process. The thermal deposition was carried out using O_2 as the oxidant gas. Film composition and stoichiometry as measured by XPS are summarized in Table I.

A clear enhancement in deposition rate and film quality is observed in the case of plasma-enhanced sALD. At 150°C the refractive index of the thermally deposited film layer is 1.82 and the C-content is relatively high, indicating a poor quality layer due to incorporation of ligand fragments in the film. Upon increasing the temperature, the refractive index for the thermal ALD process approaches the literature value of 2.19;[45] however, the GPC is still very low compared to the plasma process, as already reported for vacuum depositions.[8]

Table I. C and N contents and O/Zr ratio films for thermal (150°C) and plasma (150–250°C) deposited ZrO_2 layers, as determined by XPS measurements in the bulk films.

	N (at %)	C (at %)	O/Zr ratio
Thermal ALD @ 150°C	1.7	7.7	1.6
Plasma ALD @ 150°C	1.7	1.9	1.9
Plasma ALD @ 250°C	0.4	1.5	1.8

Table I shows that at 150°C the C content from the $N(CH_3)(C_2H_5)$ ligands is lower in the layer grown by means of O_2 plasma compared to the thermally grown layer. This is due to the highly reactive plasma species, which can efficiently oxidize and break ligand bonds resulting in desorption of C-atoms from the surface and, therefore, enhancing the film stoichiometry. Furthermore, for plasma deposited layers, the N and C contents decrease as the deposition temperature is increased from 150°C to 250°C. Once again, this can be ascribed to desorption and oxidation of ligands of the primarily adsorbed precursor species at higher temperatures as their kinetic energy approaches the activation energy for desorption.

The XRD results shown in Figure 5 reveal that film crystallinity increases with increasing deposition temperature. The thermally deposited film at 150°C is amorphous, which is in accordance with the low density of this layer denoted by the low refractive index at these conditions (*c. f.* Figure 4b). At 150°C, the plasma-deposited film is still prevalently amorphous, although a small diffraction peak can be identified at $2\theta = 35.1°$. This peak becomes more pronounced as the growth temperature increases from 175°C to 250°C. In this temperature range, a second peak appears at $2\theta = 61°$. The dependence of the crystallinity on the deposition temperature can be explained by a higher surface reactivity. By increasing the temperature, more energy is provided to the surface so that more reactive sites are activated, nucleation is promoted and the film crystallinity is enhanced. The diffraction pattern in Figure 5 may be ascribed to both cubic and tetragonal phase ZrO_2. However,

Downloaded on 2018-01-02 to IP 80.255.245.234 address. Redistribution subject to ECS terms of use (see ecsdl.org/site/terms_use) unless CC License in place (see abstract).

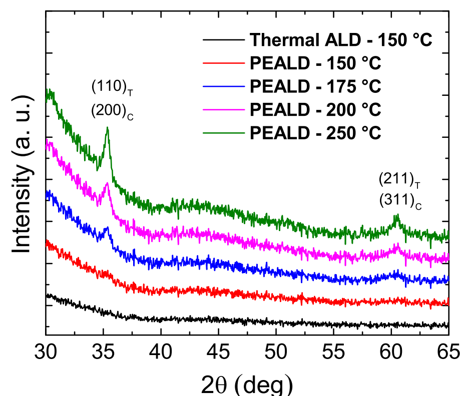

Figure 5. XRD spectra of ZrO_2 films deposited with thermal sALD at 150°C and with plasma sALD at temperatures between 150°C and 250°C. Here, the subscripts T and C refer to the tetragonal and cubic phase of the crystalline film, respectively.

tetragonal phase ZrO_2 is known to calcinate at non-stoichiometry conditions (O/Zr < 2) in N_2.[46] Therefore, considering the atmospheric pressure plasma ALD reactor as a N_2 sealed environment, the tetragonal phase seems to be in agreement with the non-stoichiometric O/Zr ratio in Table I. Moreover, according to Blanquet et al.,[37] PEALD with O_2 plasma favors the formation of tetragonal ZrO_2 due to the activation of many, small reaction sites that can grow in small crystallites due to the low surface energy associated with this phase. This would also explain why diffraction peaks of the monoclinic phase, characterized from a high surface energy, are not observed.

The optical bandgap of the ZrO_2 was extracted from transmittance and reflectance measurements (*c.f.* Supplementary Material). The energy bandgap is found to increase with the growth temperature and falls within the range between 4.8 eV and 5.8 eV. These values are consistent with the energy bandgap typically reported for tetragonal phased ZrO_2.[46–49]

Dielectric Properties

The dielectric properties of the ZrO_2 layers deposited via plasma enhanced sALD were tested in MIM capacitors, as described in the Experimental section. The layout of the capacitors used is shown in the inset of Figure 6a.

The figures of merit typically used to assess the electrical performance of thin dielectric films are their relative permittivity and breakdown field. To extract the relative permittivity, impedance measurements were performed on the MIM capacitors. The impedance and phase angle were measured as a function of frequency and a parallel RC circuit was used to calculate the geometric capacitance and dielectric loss. The impedance measurements were performed in the frequency range between 20 Hz and 100 kHz, in which parasitic effects from the test fixture and the leads can be disregarded. The real and imaginary part of the relative permittivity, averaged over 6 capacitors, are plotted in Figure 6a as a function of frequency for ZrO_2 layers grown at different deposition temperatures. Generally, the dielectric properties of a film depend on a number of factors including the deposition method, crystallinity, crystallographic orientation and quality of the film.[50] In our case, the relative permittivity is observed to increase from 17.6 to 28.3 in the temperature range from 150°C to 250°C; such a behavior is explained as the consequence of improved stoichiometry and crystallinity at higher temperatures.[35] The relative permittivity does not show any frequency dependence. In the frequency range investigated, any dielectric losses would be extrinsic, arising from microstructural defects, vacancies, dopants and impurities. In all cases, the dielectric losses, as seen from the imaginary part of the relative permittivity, ε_r'', are very low, indicating the high quality of the zirconium oxide layers. The values of the relative permittivity, as extracted at a frequency of 1 kHz, are presented in Figure 6b and summarized in Table II.

Table II. Electrical properties of ZrO_2 deposited via plasma enhanced sALD.

ZrO_2 deposition temperature (°C)	Relative permittivity @ 1 kHz	Resistivity ($\times 10^{11}$ Ω.m)	Breakdown field (MV/cm)
150	17.6 ± 0.2	2.10 ± 0.06	5.5 ± 0.2
200	19.1 ± 0.5	1.20 ± 0.50	4.9 ± 0.4
250	28.3 ± 0.1	0.73 ± 0.04	4.2 ± 0.2

The leakage through the ZrO_2 capacitors was measured by sweeping a voltage, from 0 V to 5 V, and measuring the corresponding current. The resistivity of the layers was calculated from the measured current at a bias of 4 V and the average over 6 capacitors is summarized in Table II. As previously reported,[8,9,28] the resistivity decreases slightly with increasing deposition temperature and is of the order of 10^{11} Ωm for all layers, in agreement with literature value.[51,52] The corresponding leakage current density is less than 5×10^{-8} A/cm^2.

The breakdown field is defined as the maximum limit of the electric field that a dielectric can tolerate before it becomes electrically conductive, which is also related to the bandgap of the material. For

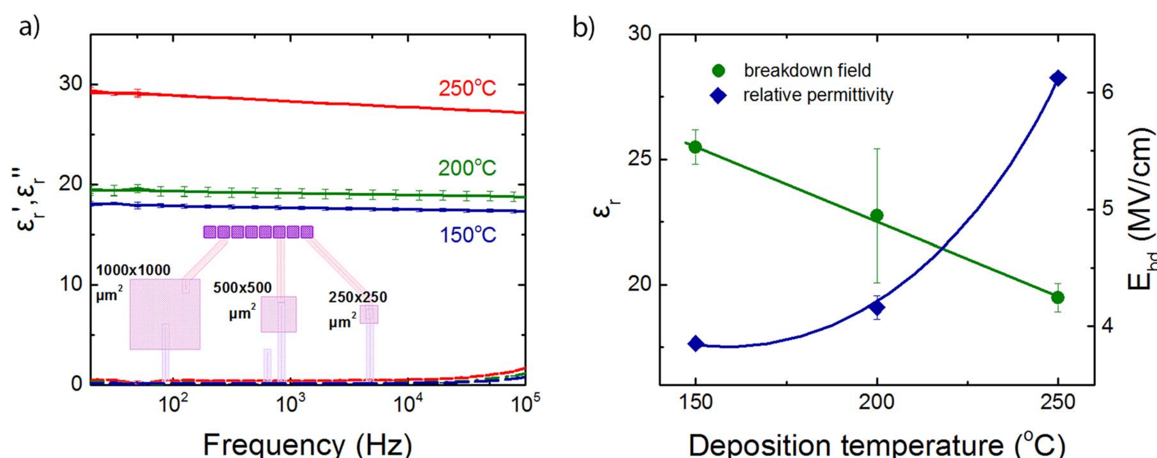

Figure 6. (a) The real, ε_r', and imaginary, ε_r'', part of the complex permittivity as a function of frequency for sALD ZrO_2 layers grown at 150°C, 200°C and 250°C, as extracted from impedance measurements. The lines represent results averaged over 6 capacitors of three different sizes, as shown in the inset. (b) Relative permittivity at 1 kHz, ε_r, and breakdown field, E_{bd}, as a function of deposition temperature. The solid lines are guides to the eye.

Downloaded on 2018-01-02 to IP 80.255.245.234 address. Redistribution subject to ECS terms of use (see ecsdl.org/site/terms_use) unless CC License in place (see abstract).

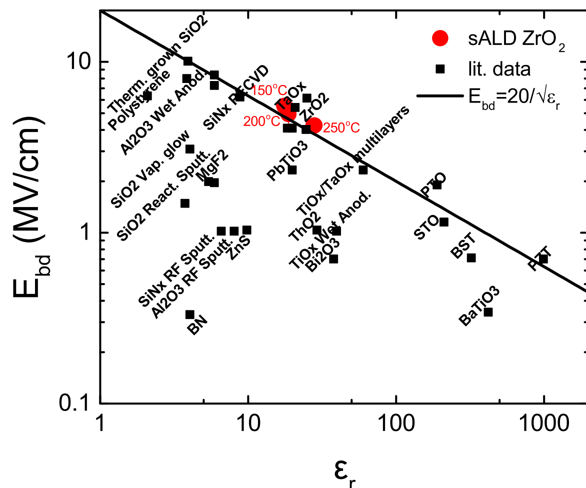

Figure 7. Breakdown field, E_{bd}, as a function of the relative permittivity, ε_r, for sALD ZrO_2 layers (red circles) and dielectrics reported in Ref. 37 (open squares). The deposition temperatures for the sALD ZrO_2 layers are indicated. The solid line represents the best-can-do empirical law $E_{bd}^2\varepsilon_r = const$. (Adapted from Ref. 38. Reprinted, with permission, from [Jain, P.; Rymaszewski, E. J. Embedded Thin Film Capacitors-Theoretical Limits. IEEE Trans. Adv. Packag. 2002, 25 (3), 454–458]).

the determination of the breakdown field, we used the ramped-voltage test. A bias sweep from 0 V to 30 V was applied and the current through the capacitors was monitored, until the breaking point, at which currents of the order of μA start flowing through the capacitors, leading to eventual mechanical failure and short-circuit formation. Ideally, the maximum breakdown field corresponds to a defect-free dielectric film. The presence of microscopic or macroscopic inhomogeneities and defects can generally lead to early breakdown. Hence, dielectric breakdown is a weakest-link problem, whose statistics are expected to follow a Weibull distribution.[53] We therefore measured 26 capacitors for each ZrO_2 layer and plotted the cumulative breakdown probability as a function of the breakdown field. The breakdown field was then taken as the value at which 50% of the capacitors breakdown. The results of this analysis are plotted in Figure 6b and summarized in Table II. The error is calculated from the lower and upper percentile lines. The average breakdown field is in the order of 5 MV/cm. As in the case of resistivity, the breakdown field decreases with increasing deposition temperature.

The decrease of the resistivity and the breakdown field with increasing deposition temperature can be linked to the increasing trend of the relative permittivity for the layers deposited at 150°C, 200°C and 250°C. As it is experimentally observed,[38] the product of the relative permittivity, ε_r, and the square of the breakdown field, E_{bd}^2, which is proportional to the electric energy density that can be stored in a dielectric material in a capacitor, is constant. This inherent trade-off between the relative permittivity and the breakdown field, or similarly the bandgap,[54] remains elusive; it has been explained as a charge-detrapping process in a dielectric film under bias.[38] Figure 7 shows the breakdown field plotted as a function of the relative permittivity for the sALD ZrO_2 layers. Literature data adapted from Ref. 37 for various dielectric materials are included. The solid line represents the empirical law $E_{bd}^2\varepsilon_r = constant,$ with the constant being ∼20.[38] Our data for sALD ZrO_2 lie on the experimentally observed best-can-do line and match previously reported data for zirconium oxide grown by means of (PE)ALD,[5,34,35,52,55,56] reactive sputtering,[57] sol-gel,[58] spray-pyrolysis[59] depositions.

Conclusions

We have investigated the growth of ZrO_2 by plasma-enhance spatial ALD at atmospheric pressure using TEMAZ and O_2 plasma as precursor and co-reactant. As compared with thermal s-ALD, PE-s-ALD deposited layers show an enhancement of the GPC up to 0.14 nm/cycle and superior layer properties within the temperature range between 150°C and 250°C. The refractive index of plasma deposited films reaches the literature value of $n = 2.1$ and the impurity content as measured by XPS decreases significantly with increasing growth temperature. XRD analysis revealed that film crystallinity also increases with the growth temperature and the obtained diffraction patterns can be attributed to both tetragonal and cubic phase ZrO_2. Furthermore, bandgap values lying in the range 4.8–5.8 eV are in agreement with literature bandgap values for tetragonal phase ZrO_2.

The electrical characteristics of ZrO_2 were investigated by embedding the layers in MIM capacitor devices. The relative permittivity as measured for layers grown at 150°C, 200°C and 250°C by PE-sALD was found to increase with deposition temperature and ranges from 17.6 to 28.3. The dielectric losses of the layers are negligible and the resistivity is on par with previously reported values for ZrO_2. The combination of breakdown field and dielectric constant lies on the experimentally observed best-can-do line, demonstrating that plasma enhanced spatial ALD at atmospheric pressure is a powerful, fast technique to deposit ultrathin, high quality dielectrics for low temperature, large scale microelectronic applications. Therefore, the integration of ZrO_2 as gate dielectric in IGZO-based TFT devices is currently under investigation.

Acknowledgments

The authors thank the process engineers of Holst Centre's GEN1 TFT Pilot Line for fabrication of the capacitors used in this paper. The research presented in this article is part of the Materials Transition Program funded by Dutch Foundation TKI HTSM. The grant for this work is labelled DGBI/14172531.

ORCID

Maria A. Mione https://orcid.org/0000-0003-1376-1565

References

1. G. E. Moore, *Electron Devices Meet. 1975 Int.*, **21**, 11 (1975).
2. D. Misra, H. Iwai, and H. Wong, *Interface*, **14**, 30 (2005).
3. E. P. Gusev, D. A. Buchanan, E. Cartier, A. Kumar, D. Di Maria, S. Guha, A. Callegari, S. Zafar, P. C. Jamison, A. A. Neumayer et al., in *Electron Devices Meeting, 2001. IEDM '01. Technical Digest. International*, p. 20.1.1 (2001).
4. J. A. Kittl, K. Opsomer, M. Popovici, N. Menou, B. Kaczer, X. P. Wang, C. Adelmann, M. A. Pawlak, K. Tomida, A. Rothschild et al. *Microelectron. Eng.*, **86**, 1789 (2009).
5. W.-J. Qi, R. Nieh, B. H. Lee, L. Kang, Y. Jeon, and J. C. Lee, *Appl. Phys. Lett.*, **77**, 3269 (2000).
6. M. Copel, M. Gribelyuk, and E. Gusev, *Appl. Phys. Lett.*, **76**, 436 (2000).
7. B. Seong, K. Kim, S. W. Lee, J. H. Han, B. Lee, and S. Han, *Adv. Funct. Mater.*, **20**, 2989 (2010).
8. S. J. Yun, J. W. Lim, and J.-H. Lee, *Electrochem. Solid-State Lett.*, **7**, F81 (2004).
9. S. Koveshnikov, N. Goel, P. Majhi, H. Wen, M. B. Santos, S. Oktyabrsky, V. Tokranov, R. Kambhampati, R. Moore, F. Zhu, J. Lee, and W. Tsai, *Appl. Phys. Lett.*, **92**, 1 (2008).
10. Y. Kamata, Y. Kamimuta, T. Ino, R. Iijima, M. Koyama, and A. Nishiyama, *Jpn. J. Appl. Phys.*, **45**, 5651 (2006).
11. J. S. Lee, S. Chang, S. M. Koo, and S. Y. Lee, *IEEE Electron Device Lett.*, **31**, 225 (2010).
12. S. M. George, *Chem. Rev.*, **110**, 111 (2010).
13. R. W. Johnson, A. Hultqvist, and S. F. Bent, *Mater. Today*, **17**, 236 (2014).
14. H. B. Profijt, S. E. Potts, M. C. M. van de Sanden, and W. M. M. Kessels, *J. Vac. Sci. Technol. A Vacuum, Surfaces, Film.*, **29**, 50801 (2011).
15. T. Suntola and J. Antson, US Pat. 4,058,430 (1977).
16. P. Poodt, D. C. Cameron, E. Dickey, S. M. George, V. Kuznetsov, G. N. Parsons, F. Roozeboom, G. Sundaram, and A. Vermeer, *J. Vac. Sci. Technol. A Vacuum, Surfaces, Film.*, **30**, 10802 (2012).
17. R. L. Z. Hoye, D. Muñoz-Rojas, S. F. Nelson, A. Illiberi, P. Poodt, F. Roozeboom, and J. L. Macmanus-Driscoll, *APL Mater.*, 3 (2015).
18. F. J. Van den Bruele, M. Smets, A. Illiberi, Y. Creyghton, P. Buskens, F. Roozeboom, and P. Poodt, *J. Vac. Sci. Technol. A Vacuum, Surfaces, Film.*, **33**, 01A131 (2015).
19. A. Illiberi, R. Scherpenborg, F. Roozeboom, and P. Poodt, *ECS J. Solid State Sci. Technol.*, **3**, P111 (2014).
20. C. H. Frijters, P. Poodt, and A. Illiberi, *Sol. Energy Mater. Sol. Cells*, **155**, 356 (2016).
21. A. Illiberi, C. Frijters, E. Balder, P. Poodt, and F. Roozeboom, *ECS Trans.*, **69**, 31 (2015).

Downloaded on 2018-01-02 to IP 80.255.245.234 address. Redistribution subject to ECS terms of use (see ecsdl.org/site/terms_use) unless CC License in place (see abstract).

22. A. Illiberi, B. Kniknie, J. Deelen, H. L. A. Van Steijvers, D. Habets, P. J. P. M. Simons, A. C. Janssen, and E. H. A. Beckers, *Sol. Energy Mater. Sol. Cells*, **95**, 1955 (2011).
23. A. Rahtu and M. Ritala, *J. Mater. Chem.*, **12**, 1484 (2002).
24. M. Ritala and M. Leskelä, *Appl. Surf. Sci.*, **75**, 333 (1994).
25. Y. Kim, J. Koo, J. Han, S. Choi, H. Jeon, and C. G. Park, *J. Appl. Phys.*, **92**, 5443 (2002).
26. K. Kukli, K. Forsgren, J. Aarik, T. Uustare, and A. Aidla, *J. Cryst. Growth*, **231**, 262 (2001).
27. M. Ritala, M. Leskelä, L. Niinistö, T. Prohaska, G. Friedbacher, and M. Grasserbauer, *Thin Solid Films*, **250**, 72 (1994).
28. K. Kukli, M. Ritala, J. Aarik, T. Uustare, and M. Leskelä, *J. Appl. Phys.*, **92**, 1833 (2002).
29. M. Putkonen, J. Niinistö, K. Kukli, T. Sajavaara, M. Karppinen, H. Yamauchi, and L. Niinistö, *Chem. Vap. Depos.*, **9**, 207 (2003).
30. J. Niinistö, M. Putkonen, L. Niinistö, K. Kukli, M. Ritala, and M. Leskelä, *J. Appl. Phys.*, **95**, 84 (2004).
31. M. Putkonen and L. Niinistö, *J. Mater. Chem.*, **11**, 3141 (2001).
32. S. J. Yun, J. W. Lim, and J. H. Lee, *Electrochem. Solid-State Lett.*, **8**, F47 (2005).
33. D. M. Hausmann, E. Kim, J. Becker, and R. G. Gordon, *Chem. Mater.*, **14**, 4350 (2002).
34. J. Koo, Y. Kim, and H. Jeon, *Japanese J. Appl. Physics, Part 1 Regul. Pap. Short Notes Rev. Pap.*, **41**, 3043 (2002).
35. J.-H. Kim, V. A. Ignatova, J. Heitmann, and L. Oberbeck, *J. Phys. D. Appl. Phys.*, **41**, 172005 (2008).
36. D. M. Hausmann and R. G. Gordon, *J. Cryst. Growth*, **249**, 251 (2003).
37. D. E. Blanquet, M. G.-J. Monnier, I. Nuta, F. Volpi, B. Doisneau, S. Coindeau, J. Roy, B. Detlefs, Y. Mi, J. ZegenHagen, C. Martinet, and C. Wyon, *ECS Trans.*, **35**, 497 (2011).
38. P. Jain and E. J. Rymaszewski, *IEEE Trans. Adv. Packag.*, **25**, 454 (2002).
39. U. Kogelschatz, *Plasma Chem. Plasma Process.*, **23**, 1 (2003).
40. P. Poodt, B. Kniknie, A. Branca, H. Winands, and F. Roozeboom, *Phys. Status Solidi - Rapid Res. Lett.*, **5**, 165 (2011).
41. P. Poodt, A. Lankhorst, F. Roozeboom, K. Spee, D. Maas, and A. Vermeer, *Adv. Mater.*, **22**, 3564 (2010).
42. T. Keuter, G. Mauer, F. Vondahlen, R. Iskandar, N. H. Menzler, and R. Vaßen, *Surf. Coatings Technol.*, **288**, 211 (2016).
43. W. Weinreich, T. Tauchnitz, P. Polakowski, M. Drescher, S. Riedel, J. Sundqvist, K. Seidel, M. Shirazi, S. D. Elliott, S. Ohsiek, E. Erben, and B. Trui, *J. Vac. Sci. Technol. A Vacuum, Surfaces, Film.*, **31**, 01A123 (2013).
44. R. L. Puurunen, W. Vandervorst, W. F. A. Besling, O. Richard, H. Bender, T. Conard, C. Zhao, A. Delabie, M. Caymax, S. De Gendt et al., *J. Appl. Phys.*, **96**, 4878, (2004).
45. Y. Imai, A. Terahara, Y. Hakuta, K. Matsui, H. Hayashi, and N. Ueno, *Eur. Polym. J.*, **45**, 630 (2009).
46. S. Chang and R. Doong, *Chem. Mater.*, **19**, 4804 (2007).
47. R. French, S. Glass, F. Ohuchi, Y. Xu, and W. Ching, *Phys. Rev. B*, **49**, 5133 (1994).
48. H. Jiang, R. I. Gomez-Abal, P. Rinke, and M. Scheffler, *Phys. Rev. B - Condens. Matter Mater. Phys.*, **81**, 1 (2010).
49. S. Vempati, F. Kayaci-Senirmak, C. Ozgit-Akgun, N. Biyikli, and T. Uyar, *J. Phys. Chem. C*, **119**, 23268 (2015).
50. J. Robertson, *Reports Prog. Phys.*, **69**, 327 (2005).
51. M. Cassir, F. Goubin, C. Bernay, P. Vernoux, and D. Lincot, *Appl. Surf. Sci.*, **193**, 120 (2002).
52. I. Kärkkänen, A. Shkabko, M. Heikkilä, J. Niinistö, M. Ritala, M. Leskelä, S. Hoffmann-Eifert, and R. Waser, *Physica Status Solidi (A) Applications and Materials Science*, **211**, 301 (2014).
53. W. Weibull, *J. Appl. Mech.*, **103**, 293 (1951).
54. A. E. Owen and J. M. Robertson, *IEEE Trans. Electron Devices*, **ED-20**, 105 (1973).
55. T. Blanquart, J. Niinistö, N. Aslam, M. Banerjee, Y. Tomczak, M. Gavagnin, V. Longo, E. Puukilainen, H. D. Wanzenboeck, and W. M. M. Kessels, *Chem. Mater.*, **25**, 3088 (2013).
56. S. J. Won, J. Y. Kim, G. J. Choi, J. Heo, C. S. Hwang, and H. J. Kim, *Chem. Mater.*, **21**, 4374 (2009).
57. B. M. Zirkl, A. Haase, A. Fian, H. Schön, C. Sommer, G. Jakopic, G. Leising, B. Stadlober, B. I. Graz, N. Gaar, R. Schwodiauer, S. Bauer-Gogonea, and S. Bauer, *Adv. Mater.*, **19**, 2241 (2007).
58. Y. Ohya, T. Kume, and T. Ban, *Japanese J. Appl. Physics, Part 1 Regul. Pap. Short Notes Rev. Pap.*, **44**, 1919 (2005).
59. G. Adamopoulos, S. Thomas, P. H. Wöbkenberg, D. D. C. Bradley, M. A. McLachlan, and T. D. Anthopoulos, *Adv. Mater.*, **23**, 1894 (2011).

Downloaded on 2018-01-02 to IP 80.255.245.234 address. Redistribution subject to ECS terms of use (see ecsdl.org/site/terms_use) unless CC License in place (see abstract).